# Nanoscale limit of the thermal conductivity in crystalline silicon carbide membranes, nanowires, and phononic crystals

Roman Anufriev, Yunhui Wu, Jose Ordonez-Miranda, Masahiro Nomura

Anufriev et al. *NPG Asia Materials* (2022)14:35
https://doi.org/10.1038/s41427-022-00382-8

NPG Asia Materials

ARTICLE Open Access

# Nanoscale limit of the thermal conductivity in crystalline silicon carbide membranes, nanowires, and phononic crystals

Roman Anufriev[1], Yunhui Wu[1], Jose Ordonez-Miranda[2] and Masahiro Nomura[1]

**Abstract**

Silicon carbide (SiC) aims to be the number one material for power microelectronics due to its remarkable thermal properties. Recent progress in SiC technology finally enabled the fabrication of crystalline SiC nanostructures. Yet, the thermal properties of SiC at the nanoscale remain overlooked. Here, we systematically study heat conduction in SiC nanostructures, including nanomembranes, nanowires, and phononic crystals. Our measurements show that the thermal conductivity of nanostructures is several times lower than that in bulk and that the values scale proportionally to the narrowest dimension of the structures. In the smallest nanostructures, the thermal conductivity reached 10% of that in bulk. To better understand nanoscale thermal transport in SiC, we also probed phonon mean free path and coherent heat conduction in the nanostructures. Our theoretical model links the observed suppression of heat conduction with the surface phonon scattering, which limits the phonon mean free path and thus reduces the thermal conductivity. This work uncovers thermal characteristics of SiC nanostructures and explains their origin, thus enabling realistic thermal engineering in SiC microelectronics.

## Introduction

The interplanetary ambitions of our civilization demand electronics working under extreme conditions of outer space and distant planets. High temperatures, intense radiation, and toxic environments are only a few of the challenges waiting for our spacecrafts on Venus or Jupiter. These challenges call for electronics powered by exceptionally resistive materials. Silicon carbide (SiC) is the material that fits the mission like no other. Tolerant to high temperatures, resistant to radiation, and chemically inert, SiC has been named "Tougher than Hell"[1] for its excellent material properties. The flip side of SiC has always been difficult fabrication technology. For decades, researchers have struggled to obtain high-quality crystalline SiC[2–4] and to adapt the top-down fabrication technology to produce micro- and nanostructures[3]. Today, the industry has almost completely mastered the fabrication of SiC nanostructures[5,6]

Yet, despite the progress in SiC nanofabrication, the nanoscale thermal properties of SiC remain overlooked. Albeit an excellent thermal conductor at the macroscale, SiC has yet to prove its ability to dissipate heat in nanostructures. For comparison, extensive research on Si shows that the thermal conductivity of nanostructures is several times lower than that of the bulk Si[7,8]. This reduction in thermal conductivity lies at the core of the overheating problem in modern Si-based microelectronics[9,10]. Thus, knowledge of nanoscale thermal properties is essential for engineering future power electronics based on SiC. However, no systematic thermal measurements have been carried out on SiC nanostructures.

Here, we aim to demonstrate how the thermal conductivity of crystalline SiC scales with the size of the structure. We systematically measure the thermal conductivity of various SiC nanostructures and correlate it to the surface scattering of phonons. Moreover, we

Correspondence: Roman Anufriev (anufriev@iis.u-tokyo.ac.jp)
[1]Institute of Industrial Science, The University of Tokyo, Tokyo 153-8505, Japan
[2]Institute Pprime, CNRS, Universite de Poitiers, ISAE-ENSMA, F-86962 Futuroscope, Chasseneuil, France

investigate whether the surface scattering reduces the phonon mean free path (MFP) or causes coherent heat conduction. Our results should help with the thermal engineering in SiC-based power devices, MEMS[11,12], emitters[13,14], transistors[1,15], nanomembranes[16,17], and other nanoarchitectures[18].

## Results

### Sample preparation and measurements

The samples were fabricated on a SiC membrane shown in Fig. 1a. The SiC membrane was suspended in a 1 × 1 mm window of Si frame that serves as a support. To verify the crystal quality of the membrane, we performed an electron backscatter diffraction (EBSD) study. The EBSD reveals the Kikuchi pattern of crystalline 3C-SiC (Fig. 1b). Also, the EBSD orientation mapping demonstrates that the crystal preserves the orientation over the entire membrane. Figure 1c–e shows uniform color maps with the (001) orientation for z-direction and (101) orientation for x and y directions over the 1 × 1 mm surface. To evaluate the surface roughness, we profiled the surface with the atomic force microscopy (AFM). The topology features surface irregularity below 1 nm, as shown in Fig. 1f. Analyzing the surface profiles, we concluded that the surface is atomically flat with r.m.s. surface roughness ($\sigma$) close to 0.2 nm—the value typically observed on polished membranes.

The nanostructures were fabricated on the SiC membrane using the standard top-down fabrication process adapted to work on rigid suspended membranes (see the "Methods" section). In brief, we deposited circular aluminum (Al) pads for the thermal conductivity measurements

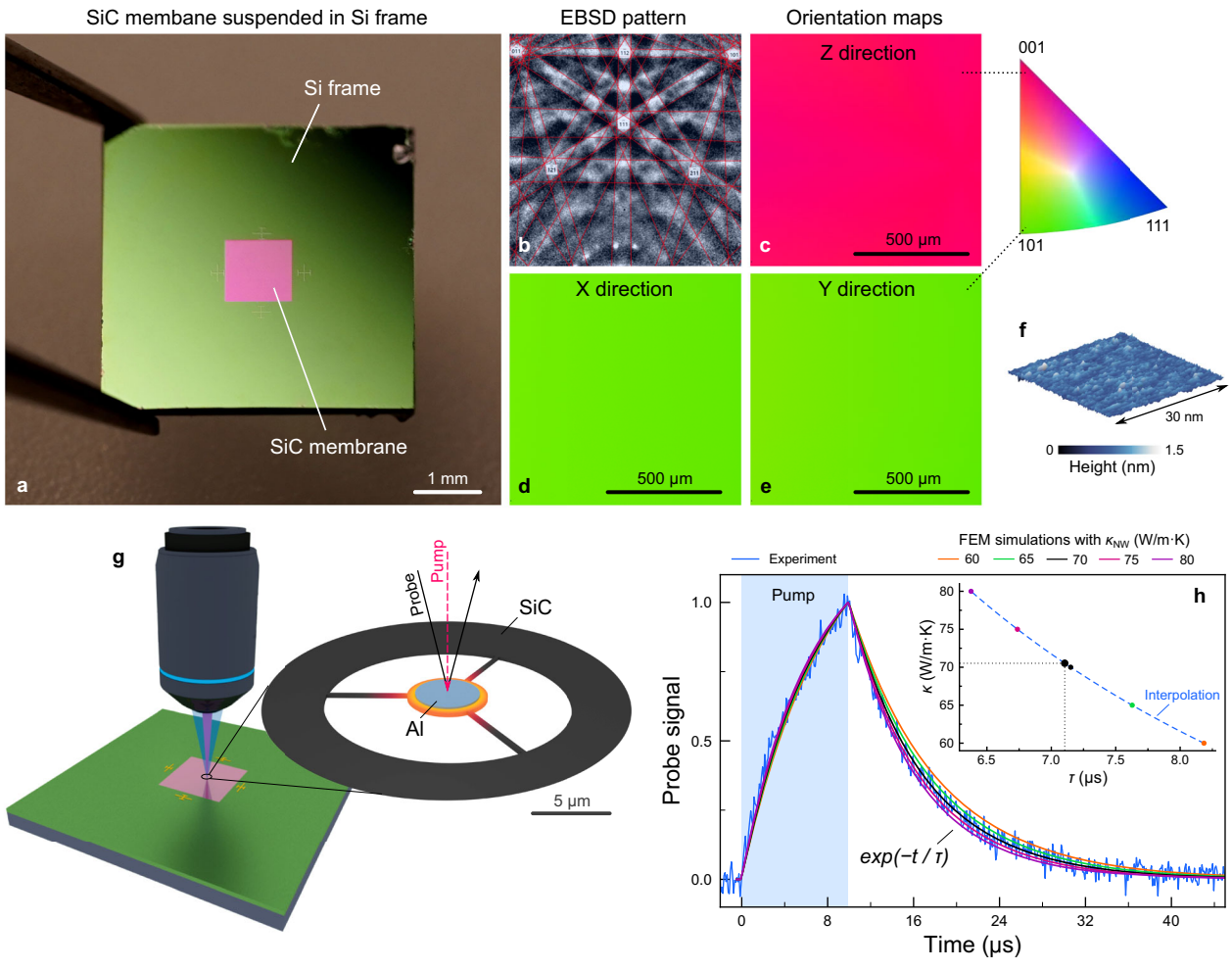


**Fig. 1 Samples and experimental method. a** Photo of a typical SiC membrane suspended in the Si frame. **b** EBSD pattern demonstrates 3C crystallinity of SiC sample. **c**–**e** EBSD maps for different directions show that the membrane preserves the crystallographic orientation over 1 × 1 mm. **f** AFM image shows low surface roughness of the membrane. **g** Scheme of the entire membrane and a typical sample on it. **h** $\mu$TDTR signal following $\exp(-t/\tau)$ reproduced by simulations. The inset shows how the simulated $\kappa(\tau)$ dependence helps to find the thermal conductivity ($\kappa$) from the measured decay time ($\tau$).

on top of the membranes. Next, using electron-beam lithography, we created patterns of nanostructures around the Al pads. Finally, the membrane was etched through the pattern in the resist. Figure 1g illustrates one of the obtained nanostructures, where the central island is supported by three nanowires.

To measure the thermal conductivity of our samples, we used the micro time-domain thermoreflectance ($\mu$TDTR) method[19–21] ("Methods"). In this pump-probe technique, pulses of the pump laser periodically heated the Al pad in the center of the sample, while the continuous-wave probe laser monitored the temperature of the Al pad using the thermoreflectance effect. Each pulse of the pump laser causes a rise in temperature followed by a gradual cooling after the end of the pulse, as shown in Fig. 1h. The cooling curve follows $\exp(-t/\tau)$, where $\tau$ is the characteristic thermal decay time of the measured sample. To extract the thermal conductivity, we compared the experimentally measured $\tau$ to those obtained using finite element method (FEM) simulations of the same sample. In the simulations, the thermal conductivity of the measured nanostructures acts as a free parameter that enables roughly reproducing the experimentally measured curve (Fig. 1h). Then, our algorithm interpolates the obtained dependence of the thermal conductivity on the decay time and finds the value that corresponds precisely to the measured decay time, as shown in the inset of Fig. 1h.

To reduce the uncertainty caused by the fabrication process, each sample was fabricated in three copies. Hence, each data point in this work is an average of three independent measurements. The error bars show the standard deviation in these measurements.

## Nanomembranes

We begin this study with a simple question of whether SiC nanomembranes have lower thermal conductivity than bulk SiC. Indeed, despite applications of crystalline SiC nanomembranes in biology[16] and electronics[17], their thermal conductivity remains unknown. Figure 2a shows a scanning electron microscopy (SEM) image of a membrane sample used for our measurements. First, we measured the thermal conductivity of membranes with thickness of 150 nm. Remarkably, the measured value of 86.4 W/m·K is about four times lower than values reported for bulk 3C-SiC (≥320 W/m·K)[22]. For comparison, Si membranes of the same thickness have thermal conductivity only twice lower than that of bulk Si[23]. On the other hand, the measured value is much higher than the 1.4 W/m·K reported for amorphous SiC thin films[22,24].

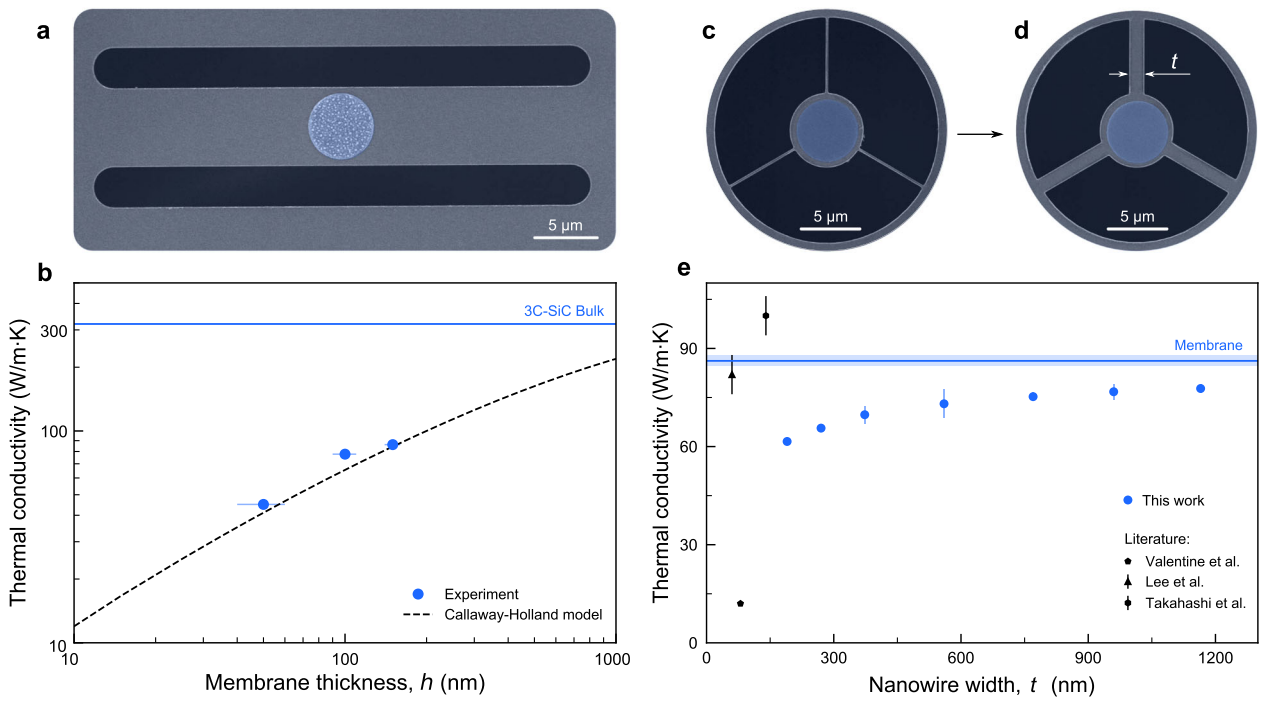


**Fig. 2 Thermal conductivity of nanomembranes and nanowires. a** SEM image of a sample for measurements of membrane thermal conductivity. **b** Measured thermal conductivity of membranes as a function of thickness at room temperature agrees with the prediction of the Callaway-Holland model. **c**, **d** SEM images of samples with narrow and wide nanowires. **e** Measured thermal conductivity of nanowires shows a trend as a function of nanowire width. For comparison, the data from literature[25–27] is shown.

Next, we thinned the membrane samples to obtain the data for the thicknesses of 100 and 50 nm. The uncertainty in the values of membrane thickness is about 10 nm. Figure 2b shows how the measured thermal conductivity decreases with the thickness. To explain the thickness dependence, we used the Callaway-Holland model ("Methods"), in which we set the membrane thickness as the dimension controlling boundary scattering rate. The trend predicted by the model matches the experimental data. Thus, the scattering of phonons on the top and bottom surfaces of the membrane can explain the reduced thermal conductivity of SiC membranes.

## Nanowires

Since one-dimensional confinement can reduce the thermal conductivity by almost an order of magnitude, we investigated if two-dimensional confinement can cause any further reduction. In the rest of the study, we fixed the thickness of all nanostructures at 150 nm. Figure 2c, d shows examples of our nanowire samples. In these samples, the island with an Al pad is suspended on three nanowires, thus making the nanowires the only heat dissipation channels. The width of these nanowires has been varied to probe how the thermal conductivity changes as one-dimensional nanowires gradually turn into wide nanoribbons. Figure 2e shows how the measured thermal conductivity becomes lower as the nanowires become narrower. For the narrowest nanowire of 190 nm in width, the thermal conductivity reaches 61.5 W/m·K, which is only 29% lower than the membrane value.

Let us now compare the measured values to those reported for SiC nanowires in the literature. Despite a wide variety of one-dimensional SiC nanostructures[6], only a few works have reported their thermal conductivity. Lee et al.[25] and Takahashi et al.[26] measured the thermal conductivity as high as 82 and 100 W/m·K on SiC nanowires with diameters of 60 and 140 nm, respectively. Conversely, Valentin et al.[27] measured values lower than 12 W/m·K for a similar nanowire of 80 nm in diameter. Simulations by Islam et al.[28] predicted 33 W/m·K for ultra-thin nanoribbon, while simulations by Papanikolaou[29] and Termentzidis et al.[30] showed only about 5 W/m·K for nanowires of a few nanometers in diameter. Thus, the present value of 61.5 W/m·K appears to be a reasonable compromise between the scattered literature data. Moreover, the measured trend with 29% reduction closely resembles that reported on Si nanowires[31,32].

## Phononic crystals

Another popular strategy to reduce the thermal conductivity is to pattern the membrane with an array of holes[33–36]. In such arrays, narrow passages between the holes can limit the phonon MFP[23,35–37]. Also, the holes might scatter phonons backward, thus further suppressing heat conduction[33]. In this regard, phononic crystals can be considered as quasi three-dimensional confinement.

Figure 3a, b shows an example of our phononic crystal sample. The holes form a periodic pattern with a square lattice of 300 nm in the period. To study the impact of the neck width ($n$), we fabricated samples with different hole diameters. The measured thermal conductivity decreases with the neck (Fig. 3c). For the narrowest neck, the thermal conductivity is as low as 33.5 W/m·K, which is an order of magnitude lower than the bulk value.

Here, we discuss the "material" thermal conductivity, which should not be confused with the "effective" thermal conductivity of porous materials often used in the literature. The material thermal conductivity already accounts for the reduced material volume and Sharvin thermal resistance[38] caused by the constrictions between the holes. Thus, the observed reduction can only be caused by internal factors, such as surface scattering.

To see if the surface scattering is indeed the leading cause of the thermal conductivity reduction, we employ the Callaway-Holland model once more. This time, we set the neck as the limiting dimension of the boundary scattering rate. Again, the predictions of the model agree with the measured trend. Thus, the phonon scattering in the narrow passages between holes appears to be the simplest explanation for the observed trend.

A similar reduction is often observed in phononic crystals made of Si[23,34,35]. For comparison, Fig. 3c also shows the thermal conductivity of Si phononic crystals with similar dimensions[20]. Remarkably, although the thermal conductivity of bulk SiC is more than twice higher than that of Si, the values of SiC and Si nanostructures are nearly the same.

Also, we measured the thermal conductivity at different temperatures. Figure 3d shows that the reduction in thermal conductivity occurs at all temperatures. The Callaway-Holland model predicts trends consistent with the experimental values in the 200–300 K range but overestimates the values at lower and higher temperatures. This discrepancy is likely caused by the uncertainty in the scattering rates obtained by Joshi et al.[39] for bulk SiC of different crystallinity and primarily for the temperatures above 300 K. Future theoretical works should precise the scattering rates for 3C-SiC at different temperatures.

## Phonon mean free path

To better understand the observed reduction in thermal conductivity, let us now discuss the phonon MFP. In general, bulk SiC has long phonon MFP as compared to other semiconductors[40,41]. For example, while in Si free paths at room temperature can be as short as 10 nm[42], free paths in SiC are longer than a few tens of nanometers and can span beyond ten microns[40,41]. However, in our previous study[43],

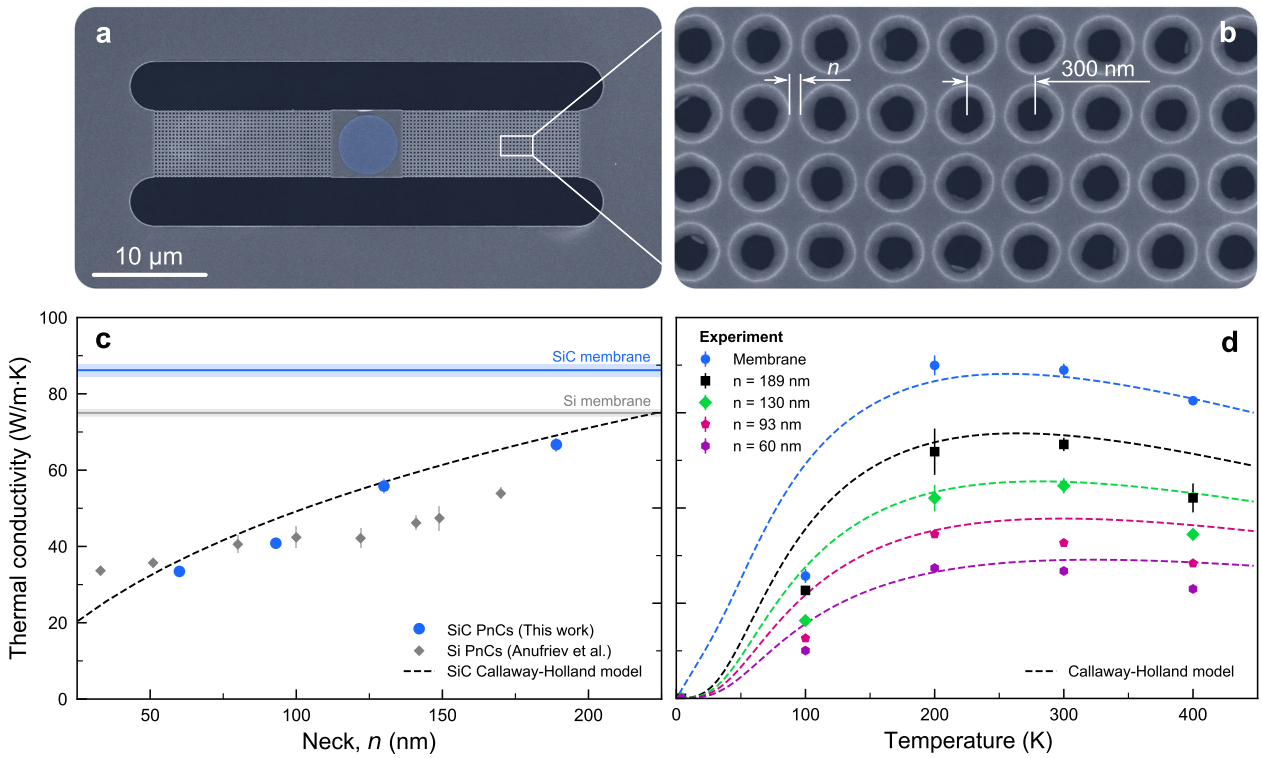


**Fig. 3 Thermal conductivity of phononic crystals. a**, **b** SEM images of a phononic crystal sample. **c** Thermal conductivity of SiC phononic crystals as a function of inter hole distance—neck—at room temperature. The trend shows the reduction in thermal conductivity as the neck narrows. The Callaway-Holland model supports the experimental data. **d** Temperature dependence of the thermal conductivity for different neck sizes.

we found that phonon MFP in thin membranes can be more than ten times shorter than that in bulk. Thus, probing MFP in our SiC membrane may be essential to explain the observed thermal conductivity reduction.

To measure the MFP spectrum of our membrane, we used the "slit method"[43,44]. We patterned the membranes with arrays of slits with different widths of the passage between the slits ($w$), as shown in Fig. 4a, b. Assuming that the narrow passages between the slits limit the phonon MFP, we can estimate the contribution of phonons with different MFP from the thermal conductivity measured for different passage widths ($w$). Note that in contrast with the previous sections, here we need to use the effective thermal conductivity normalized by the value of unpatterned membrane at each temperature, as required by the "slit method". Figure 4c shows the normalized effective thermal conductivity as a function of passage width measured at different temperatures. Naturally, as the passages narrow and reduce the phonon MFP, the thermal conductivity decreases. Moreover, the trends shift down as temperature decreases, suggesting a more substantial cut of the MFP spectra at lower temperatures.

To extract the MFP distribution from these data, we used the analytical procedure ("Methods") developed by Hao et al.[44] and improved in our previous work[43]. First, we fit the measured thermal conductivity trends to obtain the fitting coefficients. Then, using the obtained coefficient, we can reverse engineer the cumulative thermal conductivity as a function of the MFP. This function essentially shows the distribution of the phonon MFPs in the structure.

Figure 4d compares the obtained MFP distributions and reference data from the literature. At room temperature, the MFPs in the SiC membrane are substantially shorter than the MFPs in bulk SiC[41], which explains the reduced thermal conductivity in membranes. Moreover, the MFP in SiC membrane is longer than that in Si membrane[43], which explains the higher thermal conductivity in SiC membrane, albeit not the only factor. As the temperature is decreased, the MFP distribution shifts toward longer distances. This behavior is mainly caused by the lower rate of phonon–phonon scattering at lower temperatures and is consistent with previous experimental observations[42,43,45]. At 4 K, the MFP reaches the 100–700 nm range. Remarkably, this range is similar to the 70–600 nm range observed at 4 K on Si membranes of 145 nm in thickness[43]. Such similarity between membranes made of different materials occurs because phonon–phonon scattering disappears at 4 K, and the surface scattering remains the only factor limiting the MFP.

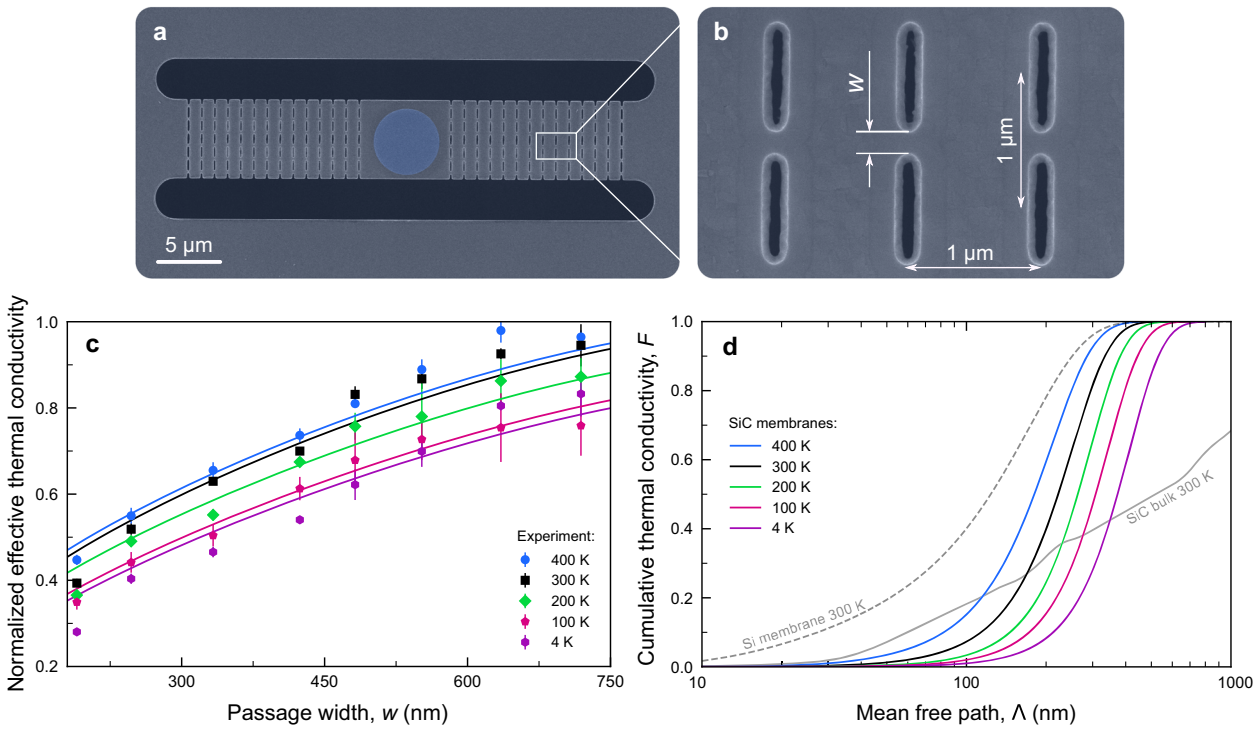


**Fig. 4 Phonon MFP in nanomembranes. a**, **b** SEM images of a sample with arrays of slits. **c** The normalized effective thermal conductivity measured as a function of the passage between the slits at different temperatures. Lines show the fits with analytical model. **d** Extracted distributions of phonon MFP at different temperatures. Data for Si membrane[43] and bulk SiC[41] are shown for comparison.

## Coherent heat conduction

Long phonon MFP at low temperatures suggests the possibility of a coherent heat conduction regime. In this regime, phonons can elastically reflect from periodic boundaries and build interference patterns, provided that their MFP is long enough[46]. Such phonon interference changes phonon properties and tends to suppress heat conduction[47,48]. The coherent regime has been demonstrated at low temperatures in Si and SiN phononic crystals[48,49]. One method to probe for the presence of the coherent regime is comparing heat conduction in nanostructures with periodic and randomized interfaces[33,49]. Figure 5a, b shows examples of our samples with ordered and disordered ($\delta = 15\%$) arrays of holes. In the disordered arrays, the shift $\Delta$ of each hole from its original position is randomized as $\Delta = \delta \cdot a \cdot \epsilon$, with $\gamma$ as the disorder coefficient, $a = 300$ nm as the period of phononic crystal, and $\epsilon$ as a random number between plus and minus one.

Figure 5c compares the normalized decay time $\tau/\tau_{\delta=0}$ measured on the samples with different disorder coefficients $\delta$ at different temperatures. At all temperatures, the decay time as a function of the disorder either remains flat or even increases by a few percent. In other words, heat dissipation becomes slightly slower in disordered lattices. Conversely, in the coherent regime, slower heat conduction

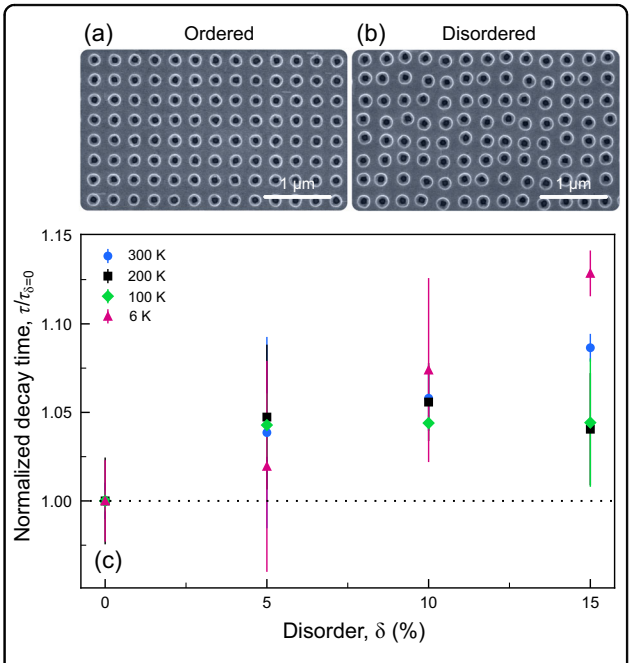


**Fig. 5 Coherent heat transport measurements.** SEM images of **a** ordered and **b** disordered phononic crystals. **c** Normalized decay time measured at different temperatures shows that heat conduction is slower in the more disordered phononic crystals. This trend suggests the absence of coherent heat conduction.

is expected in the ordered structures[49]. Thus, the observed trend ($\tau/\tau_{\delta=0} \geq 1$) is the inverse of that expected from the coherent regime ($\tau/\tau_{\delta=0} < 1$). This result implies that our experiment could not sense the presence of the coherent regime, even at low temperatures.

The slight increase in the decay time observed for disordered lattices may have several explanations. First, the path from the hot to the cold side is slightly longer in the disordered lattices, although this effect is almost negligible[20]. Second, our previous studies showed that the passages between the holes can create directional heat fluxes[50]. These directional fluxes cause faster heat dissipation in ordered lattices but are blocked by the disordered holes[20], thus slowing the heat dissipation. Third, narrowing the neck regions in disordered lattices can also suppress heat conduction[51].

## Discussion

Let us now summarize and discuss the implications of our results. First, we measured the reduced thermal conductivity in SiC nanomembranes. The reduction agreed with the Callaway-Holland model and hence was attributed to the limitation of the phonon MFP caused by surface scattering. Our measurements of MFP distributions in nanomembranes confirmed this hypothesis. The measured MFPs were substantially shorter than those in bulk, but slightly longer than those in Si membranes.

Next, we measured SiC nanowires of different widths. The narrowest nanowires showed 29% lower thermal conductivity than the membrane, in agreement with similar measurements on Si nanowires[31,32]. This result implies that the secondary confinement in nanostructures carries less weight than the primary confinement. In other words, as long as the width is larger than the thickness, the confinment in width does not substantially affect the MFP. Naturally, this changes when the secondary confinement becomes primary and the thickness is no longer the smallest dimension. Our measurements on phononic crystals showed that when the neck became smaller than the membrane thickness, the thermal conductivity can decrease substantially. In a phononic crystal with the narrowest neck, the thermal conductivity is 60% lower than in the membrane without holes and ten times lower than that in bulk. The Callaway-Holland model once again supported this finding.

Moreover, the lowest thermal conductivity in phononic crystals is also lower than that in the thinnest membrane, although the membrane thickness (50 nm) is smaller than the narrowest neck (60 nm). This implies that the size of the limiting dimension, although dominant, is not the only factor controlling the thermal conductivity. The literature often suggests coherent heat conduction as a factor causing additional reduction in the thermal conductivity of phononic crystals[48,49].

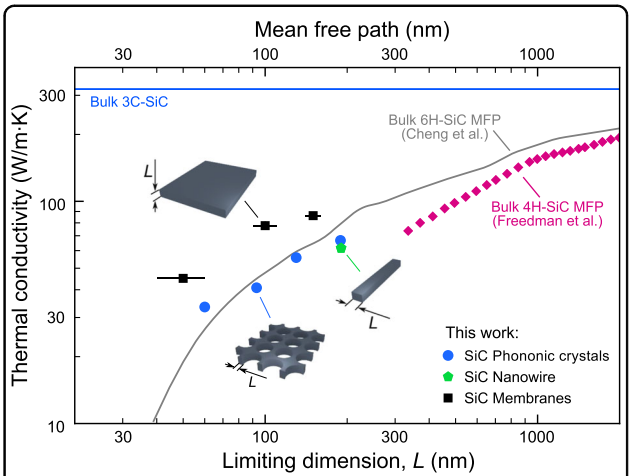


**Fig. 6 Thermal conductivity controlled by limiting dimensions.** Results of this work plotted as a function of limiting dimension show that the measured thermal conductivity values correlate with those expected from the bulk MFP accumulation functions from literature[40,41] plotted on the same graph.

Taking into account long phonon MFP measured in our samples, coherent phonon transport indeed appears plausible, at least at low temperatures. To test for the presence of coherent heat conduction, we repeated the disorder experiments from Maire et al.[49]. In contrast with the experiments on Si phononic crystals[49], our experiments showed no signs of coherent transport even at low temperatures. This difference between the results for Si and SiC is likely caused by the visibly higher surface roughness of our SiC phononic structures. Further improvements in the fabrication process might result in a more optimistic outcome.

Thus, the only explanation of the measured thermal conductivity appears to be diffuse surface scattering that limits the phonon MFP. To illustrate this conclusion, Fig. 6 summarizes the main results of our experiments. The thermal conductivity indeed correlates with the values on the calculated bulk MFP cumulative function[41] at the corresponding limiting dimensions of the nanostructures. The slightly higher values in membranes are likely due to the lower surface roughness or because MFP in membranes is not limited in the lateral plane.

To conclude, our experiments demonstrate that phonon MFP is suppressed by at least one order of magnitude and is controlled by the narrowest dimension of nanostructures. As a consequence, the thermal conductivity of SiC nanostructures is nowhere near the bulk values but is capped by values corresponding to the limiting dimension. For example, for a nanostructure with the smallest dimension of 60 nm, we obtained thermal conductivity as low as 33.5 W/m·K. Thus, our experiments provide realistic values of thermal conductivity for various types of SiC nanostructures and aim

to replace the widely cited bulk values in the design of SiC devices. Moreover, the Callaway-Holland model proved to be a reliable tool for predicting thermal conductivity and can be used to estimate values for even smaller nanostructures, such as transistors[1,15]. These results aim to help engineers and scientists better understand nanoscale heat conduction and design more efficient electronics based on SiC.

## Methods

### Sample preparation

The samples were fabricated on a commercially available single-crystalline SiC membrane suspended in a thick Si frame. First, we used the electron-beam (EB) lithography with ZEP 520A as a resist to create a pattern for Al pads. Then, we deposited 70 nm of Al using EB-assisted physical vapor deposition (Ulvac EX-300). For the second EB lithography, we coated the membrane with a double-layer resist to have better protection during etching. The room temperature reactive ion etching (Samco RIE-140AI) used the mixture of $SF_6$ and $O_2$ gasses as the etchant. The SiC membrane was first thinned down to 150 nm by etching from the back and then etched from the front through the pattern in resist to create the nanostructures around the Al pads. The remains of the resist were removed by UV-Ozone ashing.

### Measurements and error analysis

In the $\mu$TDTR setup, the samples are placed in a He-flow cryostat (4–400 K) vacuumed to $10^{-4}$ Pa to avoid convection. A pulsed pump laser (642 nm) and a continuous-wave probe laser (785 nm) are focused on the Al pad of the sample via an optical (×40) objective. Each 10-μs-long pulse of the pump laser causes a rise in the temperature of the Al pad. The temperature rise and subsequent cooling are monitored by the probe laser reflected from the pad and directed into a photodiode detector connected to a digital oscilloscope. The oscilloscope uses lock-in detection to integrate the signals over the last $10^4$ pulses (repetition rate 1 kHz), counted as one iteration. On each iteration, the system fits the cooling part of the signal with the $\exp(-t/\tau)$ function and records the value of $\tau$. This process is repeated until the standard deviation in the last 20 measured $\tau$ drops below 1%. Then, the average $\tau$ of the last 20 iterations is recorded as the value measured for the given sample. This experiment is repeated on three identical samples to reduce the uncertainty caused by the irregularity of the fabrication process. Thus, each data point in this work is calculated as an average of these three measurements, with standard deviation shown as error bars. More details on our $\mu$TDTR technique can be found in our previous works[20,21].

### Callaway-Holland model

The model calculates the thermal conductivity ($\kappa$) at a given temperature ($T$) as:

$$\kappa = \frac{1}{6\pi^2}\sum_j \int \frac{\hbar^2\omega_j^2(q)}{k_b T^2}\frac{\exp\left[\hbar\omega_j(q)/k_b T\right]}{\left(\exp\left[\hbar\omega_j(q)/k_b T\right]-1\right)^2} v_j^2(q)\tau_j(q,T)q^2 dq, \quad (1)$$

where $k_b$ is the Boltzmann constant, $\omega_j(q)$ and $v_j(q)$ are the frequency and group velocity on the branch $j$ of the SiC phonon dispersion at the wavevector $q$.

Under relaxation time approximation, the total scattering time $\tau$ is obtained using Mattheissen's rule as $\tau^{-1} = \tau_i^{-1} + \tau_u^{-1} + \tau_b^{-1} + \tau_{4p}^{-1}$, where scattering times are calculated as $\tau_i^{-1} = A\omega^4$ for impurity scattering, $\tau_u^{-1} = BT\omega^2\exp(\theta/T)$ with $\theta = 1200$ K for Umklapp scattering, $\tau_{4p}^{-1} = CT^2\omega^2$ for four-phonon processes, and $\tau_b^{-1} = (v_j(q)/L)\cdot(1-p)/(1+p)$ for boundary scattering, where $p$ is the probability of specular scattering. This probability is given by $p = \exp(-4q^2\sigma^2)$, where $\sigma$ is the surface roughness, which is set to 0.2 nm for the top and bottom surfaces and 2 nm for the hole surfaces.

From the thermal conductivity of bulk SiC, Joshi et al.[39] obtained the following parameters for the relaxation times: $A = 8.46\times10^{-45}$, $B = 6.16\times10^{-20}$, and $C = 6.9\times10^{-23}$. Finally, the parameter $L$ is the limiting dimension of the structure. We set this parameter to match the membrane thickness ($L = h$) for membrane samples and the neck size ($L = n$) for the phononic crystals. No fitting parameters were used to match the experimental data.

### Mean free path calculation

The MFP cumulative function $F(\Lambda)$ is related to the effective thermal conductivity of membrane with slits $\kappa_{\text{eff}}(w)$ normalized by that of a membrane $\kappa_{\text{mem}}$ as[44]:

$$\frac{\kappa_{\text{eff}}}{\kappa_{\text{mem}}} = H(w)a(w)\int_0^\infty \frac{F(\Lambda)d\Lambda}{\left(1+a(w)\Lambda\right)^2}, \quad (2)$$

where $a(w) = (4p/3L)\times H(w)/(w\times A)$. In this work, $L = p = 1$ μm, which is the period of the slit pattern. The parameter $A = 0.6$, as shown in our previous work on Si[43] and confirmed here for SiC. The function $H(w)$ is obtained from FEM simulations and accounts for the reduction of material volume and Sharvin thermal resistance[38] due to constrictions of heat flux lines caused by the slits. The function $F(\Lambda)$ can be described by:

$$F(\Lambda) = -\frac{\Lambda}{\alpha}W_0\left[-\frac{\alpha}{2\Lambda}\exp(-\frac{\alpha}{\Lambda})\text{erfc}(\frac{\Lambda_0-\Lambda}{\sqrt{2}\beta})\right], \quad (3)$$

where $W_0$ is the Lambert function of order zero, erfc is the complementary error function, and $\alpha$, $\beta$, and $\Lambda_0$ are fitting

parameters. Combining Eqs. (2) and (3), we obtain:

$$\frac{\kappa_{\text{eff}}}{\kappa_{\text{mem}}} = H(w)\int_0^1 G(x,\alpha',\beta',\gamma')dx, \tag{4}$$

where $\alpha' = \alpha a(w)$, $\beta' = \beta a(w)$, and $\gamma' = 1 + \Lambda_0 a(w)$ are non-dimensional parameters, $x = (1+a(\omega)\Lambda)^{-1}$, and

$$G(x,\alpha',\beta',\gamma') = \frac{1-x^{-1}}{\alpha'} W_0\left[\frac{\alpha'}{2(1-x^{-1})}\exp\left(\frac{\alpha'}{1-x^{-1}}\right)\text{erfc}\left(\frac{\gamma'-x^{-1}}{\sqrt{2}\beta'}\right)\right]. \tag{5}$$

Using Eqs. (4) and (5) to fit the experimental data in Fig. 4c, we obtain the coefficients $\alpha$, $\beta$, and $\Lambda_0$ used to reconstruct the $F(\Lambda)$ function. More details on this method can be found in our previous work[43].

**Acknowledgements**
We thank Laurent Jalabert, Saeko Tachikawa, and Ryoto Yanagisawa for their advice and assistance in sample preparation. We also thank Evgenii Sitnikov for the photo of the sample. This project was supported by PRESTO JST (No. JPMJPR19I1), CREST JST (No. JPMJCR19Q3), and Mirai JST (No. JPMJMI19A1).

**Author contributions**
R.A. fabricated and measured the samples, analyzed the data, and prepared the manuscript; Y.W. contributed to the sample fabrication and manuscript preparation; J.O.M. contributed to the data analysis and manuscript preparation; M.N. contributed to the sample design, funding acquisition, and manuscript preparation.

**Data availability**
Data and the code are available from the corresponding author on request.

**Conflict of interest**
The authors declare no competing interests.



Received: 6 December 2021 Revised: 23 February 2022 Accepted: 16 March 2022
Published online: 15 April 2022

**References**

1. Voosen, P. Tougher than hell. *Science* **358**, 984–989 (2017).
2. Nakamura, D. et al. Ultrahigh-quality silicon carbide single crystals. *Nature* **430**, 1009–1012 (2004).
3. Maboudian, R., Carraro, C., Senesky, D. G. & Roper, C. S. Advances in silicon carbide science and technology at the micro- and nanoscales. *J. Vac. Sci. Technol. A: Vac. Surf. Films* **31**, 050805 (2013).
4. Eddy, C. & Gaskill, D. Silicon carbide as a platform for power electronics. *Science* **324**, 1398–1400 (2009).
5. Sung, H.-K. et al. Vertical and bevel-structured SiC etching techniques incorporating different gas mixture plasmas for various microelectronic applications. *Sci. Rep.* **7**, 3915 (2017).
6. Chen, S., Li, W., Li, X. & Yang, W. One-dimensional SiC nanostructures: designed growth, properties, and applications. *Prog. Mater. Sci.* **104**, 138–214 (2019).
7. Takahashi, K. et al. Elastic inhomogeneity and anomalous thermal transport in ultrafine Si phononic crystals. *Nano Energy* **71**, 104581 (2020).
8. Malhotra, A. & Maldovan, M. Phononic pathways towards rational design of nanowire heat conduction. *Nanotechnology* **30**, 372002 (2019).
9. Waldrop, M. M. The chips are down for Moore's law. *Nature* **530**, 144–147 (2016).
10. Pop, E. Energy dissipation and transport in nanoscale devices. *Nano Res.* **3**, 147–169 (2010).
11. Guo, X., Xun, Q., Li, Z. & Du, S. Silicon carbide converters and mems devices for high-temperature power electronics: a critical review. *Micromachines* **10**, 406 (2019).
12. Zorman, C. A. & Parro, R. J. Micro- and nanomechanical structures for silicon carbide MEMS and NEMS. *Phys. Status Solidi B* **245**, 1404–1424 (2008).
13. Lukin, D. M. et al. 4H-silicon-carbide-on-insulator for integrated quantum and nonlinear photonics. *Nat. Photon.* **14**, 330–334 (2020).
14. Lohrmann, A. et al. Single-photon emitting diode in silicon carbide. *Nat. Commun.* **6**, 7783 (2015).
15. Han, J.-W., Seol, M.-L., Moon, D.-I., Hunter, G. & Meyyappan, M. Nanoscale vacuum channel transistors fabricated on silicon carbide wafers. *Nat. Electron.* **2**, 405–411 (2019).
16. Nguyen, T.-K. et al. Superior robust ultrathin single-crystalline silicon carbide membrane as a versatile platform for biological applications. *ACS Appl. Mater. Inter.* **9**, 41641–41647 (2017).
17. Phan, H.-P. et al. Long-lived, transferred crystalline silicon carbide nanomembranes for implantable flexible electronics. *ACS Nano* **13**, 11572–11581 (2019).
18. Xu, M. et al. Recent advances and challenges in silicon carbide (SiC) ceramic nanoarchitectures and their applications. *Mater. Today Commun.* **28**, 102533 (2021).
19. Maire, J. & Nomura, M. Reduced thermal conductivities of Si one-dimensional periodic structure and nanowire. *Jap. J. Appl. Phys.* **53**, 06JE09 (2014).
20. Anufriev, R., Ramiere, A., Maire, J. & Nomura, M. Heat guiding and focusing using ballistic phonon transport in phononic nanostructures. *Nat. Commun.* **8**, 15505 (2017).
21. Anufriev, R., Gluchko, S., Volz, S. & Nomura, M. Quasi-ballistic heat conduction due to Lévy phonon flights in silicon nanowires. *ACS Nano* **12**, 11928–11935 (2018).
22. Jeong, T., Zhu, J.-G., Mao, S., Pan, T. & Tang, Y. J. Thermal characterization of SiC amorphous thin films. *Int. J. Thermophys.* **33**, 1000–1012 (2012).
23. Anufriev, R., Maire, J. & Nomura, M. Reduction of thermal conductivity by surface scattering of phonons in periodic silicon nanostructures. *Phys. Rev. B* **93**, 045411 (2016).
24. Choi, S. R., Kim, D., Choa, S.-H., Lee, S.-H. & Kim, J.-K. Thermal conductivity of ALN and SiC thin films. *Int. J. Thermophys.* **27**, 896–905 (2006).
25. Lee, K.-M., Lee, S.-K. & Choi, T.-Y. Highly enhanced thermoelectric figure of merit of a β-SiC nanowire with a nanoelectromechanical measurement approach. *Appl. Phys. A* **106**, 955–960 (2012).
26. Takahashi, K. et al. Thermal conductivity of SiC nanowire formed by combustion synthesis. *High Temp. High Press.* **37**, 119–125 (2008).
27. Valentín, L. et al. A comprehensive study of thermoelectric and transport properties of β-silicon carbide nanowires. *J. Appl. Phys.* **114**, 184301 (2013).
28. Islam, M. S. et al. Molecular dynamics study of thermal transport in single-layer silicon carbide nanoribbons. *AIP Adv.* **10**, 015117 (2020).
29. Papanikolaou, N. Lattice thermal conductivity of SiC nanowires. *J. Phys.Condens. Matter* **20**, 135201 (2008).
30. Termentzidis, K. et al. Modulated SiC nanowires: molecular dynamics study of their thermal properties. *Phys. Rev. B* **87**, 125410 (2013).
31. Park, W. et al. Phonon conduction in silicon nanobeams. *Appl. Phys. Lett.* **110**, 213102 (2017).
32. Yang, L. et al. Thermal conductivity of individual silicon nanoribbons. *Nanoscale* **8**, 17895–17901 (2016).
33. Lee, J. et al. Investigation of phonon coherence and backscattering using silicon nanomeshes. *Nat. Commun.* **8**, 14054 (2017).
34. Graczykowski, B. et al. Thermal conductivity and air-mediated losses in periodic porous silicon membranes at high temperatures. *Nat. Commun.* **8**, 415 (2017).
35. Lim, J. et al. Simultaneous thermoelectric property measurement and incoherent phonon transport in holey silicon. *ACS Nano* **10**, 124–132 (2016).
36. Tambo, N. et al. Ultimate suppression of thermal transport in amorphous silicon nitride by phononic nanostructure. *Sci. Adv.* **6**, eabc0075 (2020).
37. Nomura, M., Nakagawa, J., Sawano, K., Maire, J. & Volz, S. Thermal conduction in Si and SiGe phononic crystals explained by phonon mean free path spectrum. *Appl. Phys. Lett.* **109**, 173104 (2016).
38. Prasher, R. Predicting the thermal resistance of nanosized constrictions. *Nano Lett.* **5**, 2155–2159 (2005).
39. Joshi, R., Neudeck, P. & Fazi, C. Analysis of the temperature dependent thermal conductivity of silicon carbide for high temperature applications. *J. Appl. Phys.* **88**, 265–269 (2000).

40. Freedman, J. P. et al. Universal phonon mean free path spectra in crystalline semiconductors at high temperature. *Sci. Rep.* **3**, 2963 (2013).
41. Cheng, Z. et al. Quasi-ballistic thermal conduction in 6H-SiC. *Mater. Today Phys.* **20**, 100462 (2021).
42. Regner, K. T. et al. Broadband phonon mean free path contributions to thermal conductivity measured using frequency domain thermoreflectance. *Nat. Commun.* **4**, 1640 (2013).
43. Anufriev, R., Ordonez-Miranda, J. & Nomura, M. Measurement of the phonon mean free path spectrum in silicon membranes at different temperatures using arrays of nanoslits. *Phys. Rev. B* **101**, 115301 (2020).
44. Hao, Q., Xiao, Y. & Chen, Q. Determining phonon mean free path spectrum by ballistic phonon resistance within a nanoslot-patterned thin film. *Mater. Today Phys.* **10**, 100126 (2019).
45. Zeng, L. et al. Measuring phonon mean free path distributions by probing quasiballistic phonon transport in grating nanostructures. *Sci. Rep.* **5**, 17131 (2015).
46. Maldovan, M. Phonon wave interference and thermal bandgap materials. *Nat. Mater.* **14**, 667–674 (2015).
47. Anufriev, R. & Nomura, M. Reduction of thermal conductance by coherent phonon scattering in two-dimensional phononic crystals of different lattice types. *Phys. Rev. B* **93**, 045410 (2016).
48. Zen, N., Puurtinen, T. A., Isotalo, T. J., Chaudhuri, S. & Maasilta, I. J. Engineering thermal conductance using a two-dimensional phononic crystal. *Nat. Commun.* **5**, 3435 (2014).
49. Maire, J. et al. Heat conduction tuning using the wave nature of phonons. *Sci. Adv.* **3**, e1700027 (2017).
50. Anufriev, R. & Nomura, M. Ray phononics: thermal guides, emitters, filters, and shields powered by ballistic phonon transport. *Mater. Today Phys.* **15**, 100272 (2020).
51. Romano, G. & Kolpak, A. M. Directional phonon suppression function as a tool for the identification of ultralow thermal conductivity materials. *Sci. Rep.* **7**, 44379 (2017).